Hindawi Publishing Corporation
International Journal of Photoenergy
Volume 2016, Article ID 5195138, 12 pages
http://dx.doi.org/10.1155/2016/5195138

Research Article

Effective Carbon Dioxide Photoreduction over Metals (Fe-, Co-, Ni-, and Cu-) Incorporated TiO_2/Basalt Fiber Films

Jeong Yeon Do,[1] Byeong Sub Kwak,[1] Sun-Min Park,[2] and Misook Kang[1]

[1]*Department of Chemistry, College of Science, Yeungnam University, Gyeongsan, Gyeongbuk 38541, Republic of Korea*
[2]*Korea Institute of Ceramic Engineering and Technology (KICET), Jinju, Gyeongnam 52851, Republic of Korea*

Correspondence should be addressed to Sun-Min Park; psm@kicet.re.kr and Misook Kang; mskang@ynu.ac.kr

Received 11 December 2015; Revised 15 February 2016; Accepted 22 March 2016

Academic Editor: Jennifer Strunk

Mineralogical basalt fibers as a complementary adsorbent were introduced to improve the adsorption of CO_2 over the surfaces of photocatalysts. TiO_2 photocatalysts (M-TiO_2) incorporated with 5.0 mol.% 3d-transition metals (Fe, Co, Ni, and Cu) were prepared using a solvothermal method and mixed with basalt fibers for applications to CO_2 photoreduction. The resulting 5.0 mol.% M-TiO_2 powders were characterized by X-ray diffraction, scanning electron microscopy, ultraviolet-visible spectroscopy, photoluminescence, Brunauer, Emmett, and Teller surface area, and CO_2-temperature-programmed desorption. A paste composed of two materials was coated and fixed on a Pyrex plate by a thermal treatment. The 5.0 mol.% M-TiO_2/basalt fiber films increased the adsorption of CO_2 significantly, indicating superior photocatalytic behavior compared to pure TiO_2 and basalt fiber films, and produced 158~360 μmol g_{cat}^{-1} L^{-1} CH_4 gases after an 8 h reaction. In particular, the best performance was observed over the 5.0 mol.% Co-TiO_2/basalt fiber film. These results were attributed to the effective CO_2 gas adsorption and inhibition of photogenerated electron-hole pair recombination.

1. Introduction

To mitigate the greenhouse effect, there has been increasing interest in converting the greenhouse gas, carbon dioxide (CO_2), to useful molecules, such as carbon monoxide (CO) [1, 2], methane (CH_4) [3, 4], formic acid (HCOOH) [5], formaldehyde (HCHO) [6], or methanol (CH_3OH) [7, 8], via chemical routes. On the other hand, because CO_2 is a chemically stable compound owing to its carbon-oxygen double bonds, its conversion to some hydrocarbons requires substantial energy input for bond cleavage [9]. Solar energy provides a readily available and continuous energy supply that would be suitable to drive this conversion process. In CO_2 photocatalysis to synthesize some fuels, semiconductor materials with an appropriate band-gap (the energy region extending from the bottom of the empty conduction band to the top of the occupied valence band) are required as photocatalysts. When a semiconductor photocatalyst absorbs light in a typical photocatalytic process, an electron is excited from the fully occupied valence band of the semiconductor to a higher energy empty conduction band, forming an electron-hole pair [10, 11]. These charge carriers can also recombine on the surface or in the bulk before reacting with adsorbed species, dissipating the energy as heat or light. The photoreactions occur continually with electron accepting or donating species adsorbed on the surface of the semiconductor photocatalyst. Therefore, electron-hole recombination must be minimized for photocatalytically induced redox reactions to take place [12–14].

The TiO_2 semiconductor has been assessed for CO_2 photoreduction because of its chemical stability and natural abundance. Although TiO_2 has several unique features, its use has been limited by its large band-gap (3.2 eV), meaning it can only be activated by ultraviolet light, which comprises 2–5% of sunlight [15, 16], and the relatively fast recombination between the electron and holes [17, 18]. Therefore, the photocatalyst should have a lower band-gap and an increased lifetime of the photogenerated electrons and holes through effective charge carrier separation and the suppression of electron-hole recombination. The photocatalytic activity for visible light can be increased by coupling semiconductors of different energy levels or doping with metals or nonmetals

to suppress the recombination rate and increase the quantum yield [19, 20]. Considerable efforts have been made to extend the adsorption of reactive species and the utilization of the incident light properties of catalysts to improve their photocatalytic efficiency. The approaches of combining TiO_2 with a support, such as porous materials, polycrystalline fibers, or tube materials (e.g., CNTs or polymers, magnetic materials, and minerals), to achieve charge separation and the adsorption of reactive species, have decreased the recombination rate and maintained excellent catalytic activity [21, 22].

Therefore, this study examined whether a mineral, basalt fiber [23] as a complementary material, would be sufficient to facilitate both electron-hole charge separation and CO_2 adsorption. Basalt is one of the most common rock types in the world and is found widely in large igneous provinces. Basalt contains MgO, CaO, Fe_2O_3, TiO_2, Al_2O_3, and SiO_2 and can be used as a substrate mineral to adsorb carbon dioxide. Another objective in this study was to examine the effects of 3d-transition metals as a cocatalyst in the TiO_2 photocatalytic system. In general, 3d-transition metals with excellent oxidation-reducing power are often used as thermal catalysts in some redox reactions. In particular, Ni, Co, Fe, and Cu have been applied widely as the main catalytic species from CO_2 or CO to methanol or hydrocarbons, so-called Fischer-Tropsch synthesis [24–26]. Consequently, this study examined the synergistic effects of a basalt mineral absorbent (YJC com., Hampyeong, Jeonnam, Republic of Korea) and adding transition metals (Fe, Co, Ni, and Cu) to the TiO_2 anatase framework on its properties as a photosensitizer for the photoreduction of CO_2 to CH_4.

2. Experimental

2.1. Preparation and Characterization of Nanosized 5.0 mol.% M (Fe-, Co-, Ni-, and Cu-) TiO_2 Powders and 5.0 mol.% M-TiO_2/Basalt Fiber Films. Before the design of the 5.0 mol.% M (Fe-, Co-, Ni-, and Cu-) TiO_2/basalt fiber films, four types of 5.0 mol.% M-TiO_2 powders were prepared using a solvothermal treatment [27]. Titanium tetraisopropoxide (TTIP, 99.95%, Junsei Chem. Co., Japan) and metal nitrates ($M(NO_3)_2xH_2O$, M = Fe, Ni, Co, and Cu, 99.9%, Junsei Chem. Co., Japan) were used as the precursors for titanium and other metals, respectively, and absolute ethanol was used as the solvent. After adding 0.095 M of TTIP to 250 mL of absolute ethanol in a 500 mL beaker, 0.4 M of distilled water was dropped carefully and slowly into the solution with stirring for 1 h to avoid aggregation by rapid hydrolysis, and 0.005 M (5.0 mol.%) of the metal precursors was then added to the solution. The final solution was stirred continuously for 2 h at room temperature and moved to an autoclave for thermal treatment at 200°C for 8 h under a nitrogen atmosphere at a pressure of approximately 10.0 atm. The resulting precipitate was washed with distilled water until the pH was 7.0 and dried at 50°C for 24 h. The pure TiO_2 nanoparticles were also obtained using the same method. The prepared TiO_2 and 5.0 mol.% M-TiO_2 were used as the main photocatalytic species for CO_2 reduction.

For the design of 5.0 mol.% M-TiO_2/basalt fiber films for application to the CO_2 photoreduction reaction, the basalt fibers were ground to a small size, and 70–100 mesh-sized powders were filtered and selected for use as the support substrate. The paste was composed of 2.0 g of 5.0 mol.% M-TiO_2 powders and basalt fiber pieces with a mixture containing 5.0 g of α-terpineol, 0.5 g of cellulose, and 20 mL of ethanol. The paste was then sonicated for 24 h at 1,200 Wcm^{-3}. Subsequently, a Pyrex plate was coated with the mixed paste with the M-TiO_2 powders and basalt fiber pieces using a squeeze printing technique. The size of the formulated 5.0 mol.% M-TiO_2/basalt fiber films was 8.0 mm × 5.0 mm. The 5.0 mol.% M-TiO_2/basalt fiber films were then heat treated at 450°C for 30 minutes to remove the additives.

The synthesized 5.0 mol.% M-TiO_2 powders were examined by X-ray diffraction (XRD, MPD, PANalytical) using nickel-filtered CuKα radiation (30 kV, 30 mA). The reflectance UV-vis spectra of the 5.0 mol.% M-TiO_2 powders were obtained using a Cary 500 spectrometer with a reflectance sphere in the range 200~800 nm. The Brunauer, Emmett, and Teller (BET) surface areas of the 5.0 mol.% M-TiO_2 powders were measured using a Belsorp II instrument. The recombination tendency of the photogenerated electron-hole pairs (e^-/h^+) in 5.0 mol.% M-TiO_2 powder was estimated by photoluminescence (PL, Photoluminescence Spectrometer, PerkinElmer) spectroscopy using a He-Cd laser source at a wavelength of 325 nm. The adsorption of CO_2 on the 5.0 mol.% M-TiO_2 powders was measured from CO_2-TPD (temperature-programmed desorption) experiments in the same manner used for thermogravimetric analysis (TGA, Sinco Co., Republic of Korea).

The morphology of the 5.0 mol.% M-TiO_2/basalt fiber films was observed by scanning electron microscopy (SEM, JEOL 2000EX) and the atomic compositions of the films were determined by energy-dispersive X-ray spectroscopy (EDAX, EX-250, Horiba).

2.2. Photocatalytic Activities over 5.0 mol.% M (Fe-, Co-, Ni-, and Cu-) TiO_2/Basalt Fiber Films. A batch type photoreactor was designed in the laboratory, as shown in Figure 1. The reactor consisted of a rectangular quartz cell with a total volume of 60.0 mL. The photocatalytic activity was examined using the formulated 5.0 mol.% M (Fe-, Co-, Ni-, and Cu-) TiO_2/basalt fiber films (8.0 × 5.0 mm^2 size) fixed uniformly to the bottom of the reaction chamber. A 1.0 mm thick quartz glass window cover was placed on the top of the reactor to enable the effective transfer of irradiation from two 6.0-W/cm^2 mercury lamps with a 365 nm wavelength. The reactor chamber and lamp were covered with aluminum foil to ensure that all the radiation that participated in the reaction had passed through the quartz window. The reactor, which had been checked for leakage at atmospheric pressure for several hours, was purged with helium carrier gas. The reaction temperature and pressure were maintained at 313 K and 1.0 atm, respectively. Before starting the experiment, the reactor was purged for one hour with a mixture of CO_2 and helium. The $CO_2 : H_2O$ ratio was fixed to 1 : 2. During the photocatalysis process, the product mixture was sampled

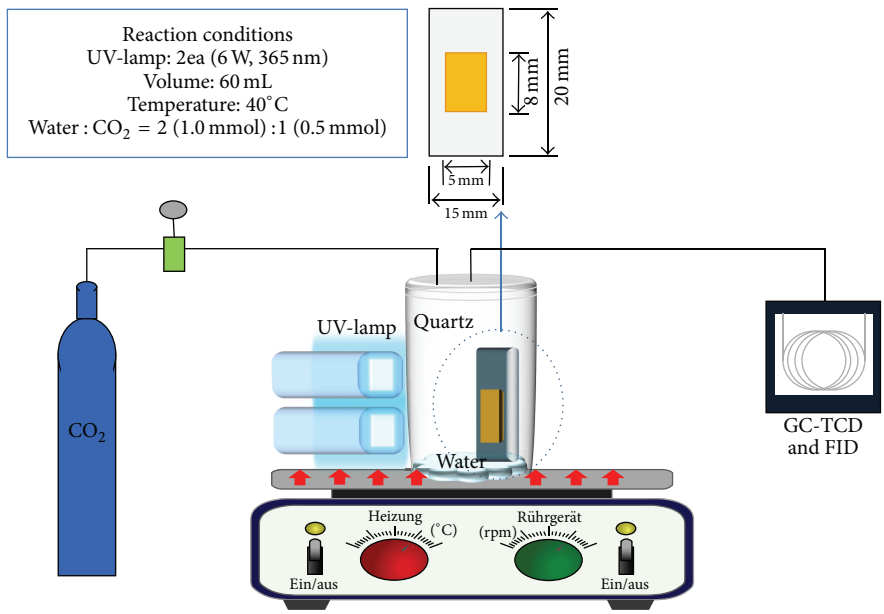

FIGURE 1: Batch type photoreactor used for CO_2 photoreduction to CH_4.

off-line using a gas tight syringe (Agilent, 250 μm) with the same volume and analyzed by gas chromatography (GC, iGC7200, Donam Co., Republic of Korea) equipped with a thermal conductivity detector (TCD) and a flame-ionized detector (FID). First, the gaseous products produced by the in situ system were flowed into the TCD detector that was connected to a Carboxen 1000 (Young Lin Instrumentals Co., Republic of Korea) column to analyze the light gases (H_2, O_2, CO, CO_2, CH_3OH, and CH_3COOH). The extracted gases were then inserted into the FID detector to separate the C_1 (methane)–C_3 light hydrocarbons. The selectivity of the product was calculated using the following equation: C_i (%) = C_i moles in product/total moles of C produced × 100.

3. Results and Discussion

3.1. Physical Properties of the 5.0 mol.% M (Fe-, Co-, Ni-, and Cu-) TiO_2 Powders. Figure 2 presents XRD patterns of the basalt fiber, pure TiO_2, and 5.0 mol.% M (Fe-, Co-, Ni-, and Cu-) TiO_2 powders. All the peaks for the 5.0 mol.% M-TiO_2 powders were assigned to the anatase TiO_2 tetragonal structure [28]. The XRD patterns showed the main peaks at 25.35°, 37.79°, 48.08°, 53.92°, 55.12°, 62.73°, 68.60°, 70.36°, 75.09°, 83.14°, and 95.18° 2θ, which were assigned to the (d101), (d004), (d200), (d105), (d211), (d204), (d116), (d220), (d215), (d312), and (d321) planes, respectively. Depending on the addition of other transition metals to the TiO_2 framework, the peak intensities decreased slightly with some broadening. On the other hand, no peaks were observed for the added metals oxide forms, which mean that the metal ions had been well-inserted into the TiO_2 framework. Generally, peak broadening indicates a decrease in crystallite size [29]. Peak broadening of the d101 peak is related to the crystallite size of the tetragonal crystalline phase of anatase. Debye-Scherrer's equation [30] was used to determine the crystallite size and lattice strain. Based on the full width at half maximum height of the d101 peak, the crystallite sizes (lattice strains) for TiO_2 and 5.0 mol.% Fe-, Co-, Ni-, and Cu-TiO_2 were 13 (0.013) and 14 (0.012), 14 (0.012), 16 (0.010), and 17 (0.009) nm, respectively.

Figures 3(a) and 3(b) show the UV-visible absorption spectra and their Tauc's plots of the prepared 5.0 mol.% M (Fe-, Co-, Ni-, and Cu-) TiO_2 powders. An absorption band for the anatase structured TiO_2 (Figure 3(a)) was observed in the UV-region around 378 nm when extrapolated, which is similar to the absorption wavelength reported elsewhere [31]. According to the addition of transition metal species, there are different absorption band shifts, which were shifted to higher wavelengths compared to the absorption band of TiO_2. The 5.0 mol.% M-TiO_2 samples showed broad curves for the metal oxides in the visible region; the maximum absorption was observed at 490, 580, 700 (too broad), and 650 (too broad) nm for 5.0 mol.% Fe-, Co-, Ni-, and Cu-TiO_2, respectively. These bands can convert to the following absorption terms using Tanabe-Sugano's energy absorption [32]: $^5T_{2g} \rightarrow {}^5E_g$ for d^6-FeO, $^4T_{1g} \rightarrow {}^4T_{2g}$ for d^7-CoO, $^3A_{2g} \rightarrow {}^3T_{2g}$ for d^8-NiO, and $^2E_g \rightarrow {}^2T_{2g}$ for the d^9 electron configuration CuO. Generally, the band-gap in a semiconductor material is closely related to the wave range absorbed: the larger the absorption wavelength, the narrower the band-gap [33]. Using Tauc's equation [34], the band-gaps for the absorption of TiO_2 and 5.0 mol.% Fe-, Co-, Ni-, and Cu-TiO_2 in the UV-region were estimated to be 3.18 and 2.80, 2.48, 2.98, and 3.10 eV, respectively, as shown in Figure 3(b). The inserted transition metals could alter the band-gap of TiO_2 significantly, leading to easy absorption and eventually efficient photocatalysis.

Figure 4 presents the PL spectra of the prepared 5.0 mol.% M (Fe-, Co-, Ni-, and Cu-) TiO_2 particles. The PL curve

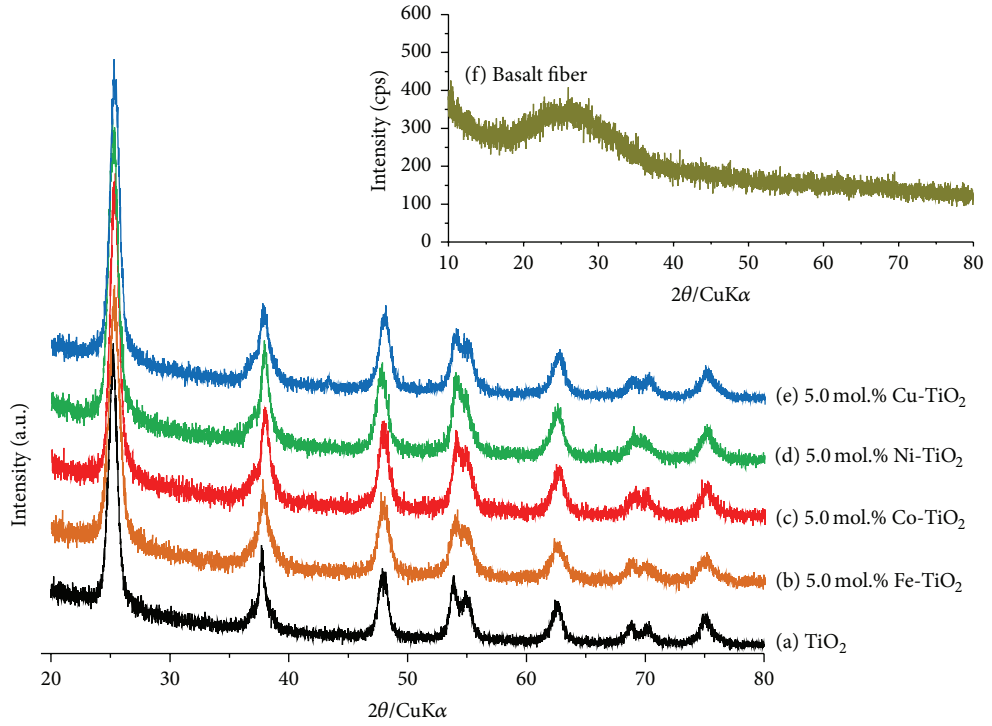

FIGURE 2: XRD patterns of the basalt fiber, pure TiO_2, and 5.0 mol.% M-TiO_2 powders.

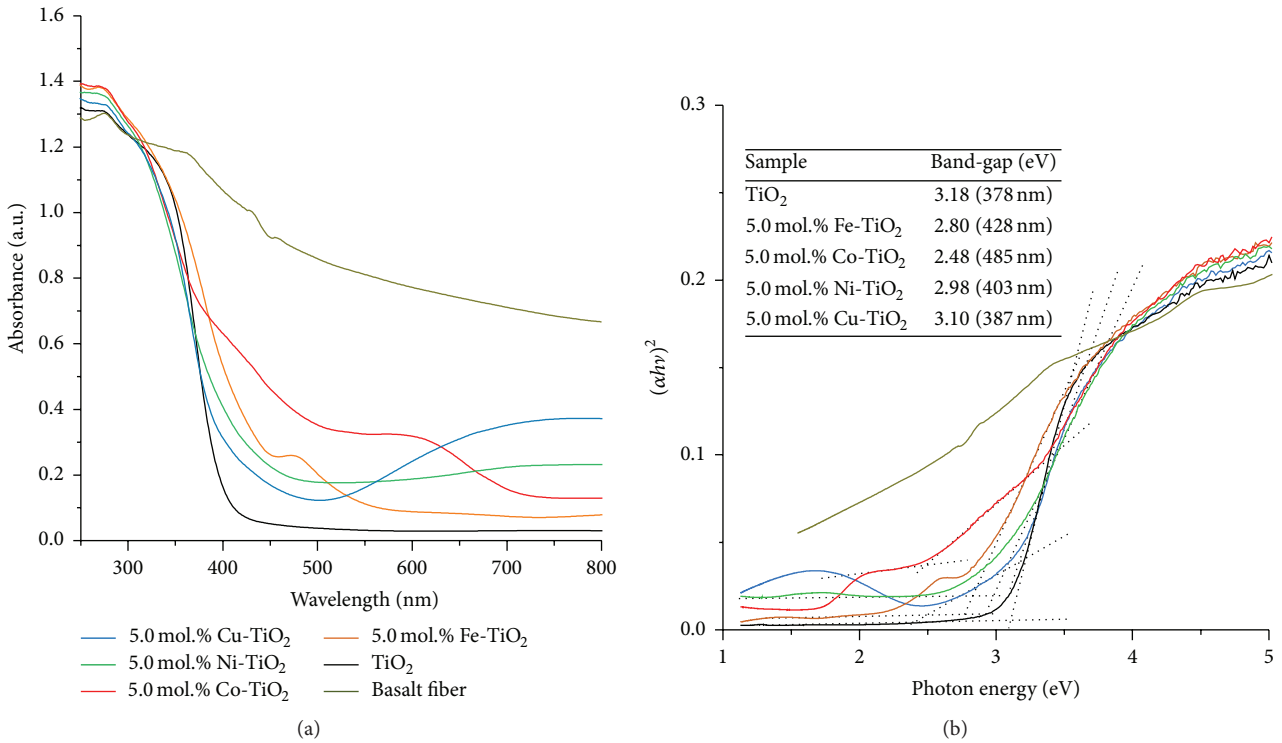

FIGURE 3: Diffuse reflectance-UV-visible absorption spectra (a) and their Tauc's plots (b) of the prepared 5.0 mol.% M-TiO_2 powders.

Table 1: Physical properties of 5.0 mol.% M-TiO_2 particles.

Physical properties of catalysts	Atomic compositions Ti : M : O	Specific surface areas [$m^2\ g^{-1}$]	Total pore volume [$cm^3\ g^{-1}$]	Average pore diameter [nm]
TiO_2	32.0 : 0.0 : 68.0	131	0.20	6.17
5.0 mol.% Fe-TiO_2	30.2 : 3.7 : 66.0	165	0.64	15.56
5.0 mol.% Co-TiO_2	30.6 : 3.4 : 67.0	124	0.17	5.63
5.0 mol.% Ni-TiO_2	28.9 : 3.1 : 68.0	130	0.18	5.63
5.0 mol.% Cu-TiO_2	31.6 : 2.9 : 65.5	67	0.42	24.95

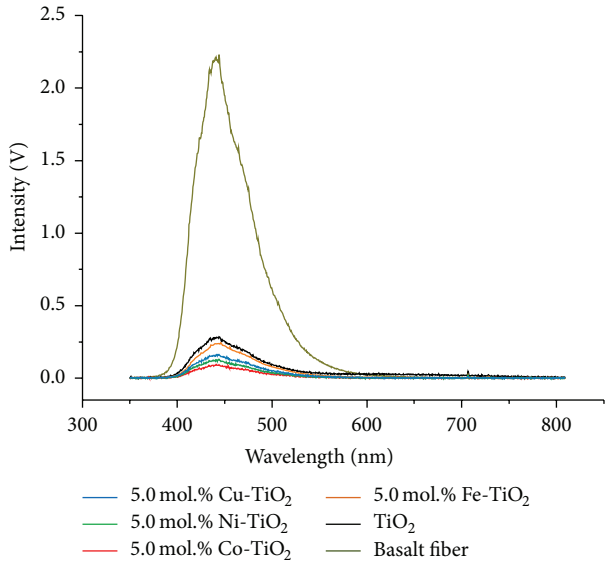

Figure 4: PL spectra of the prepared 5.0 mol.% M-TiO_2 particles.

suggests that the electrons in the valence band are transferred to the conduction band and are stabilized by photoemission. In general, the PL intensity increases with increasing number of electrons emitted, resulting from recombination between the excited electrons and holes, and a consequent decrease in photoactivity [35]. Therefore, there is a strong relationship between the PL intensity and photoactivity. In particular, the PL intensity decreases significantly when a metal can capture excited electrons or exhibit conductivity, which is known as the relaxation process. The 5.0 mol.% M-TiO_2 samples exhibited a PL signal with a similar curve shape, demonstrating the presence of TiO_2. Pure TiO_2 exhibited a strong PL signal in the range 400–550 nm, with a maximum excitation wavelength of 445 nm, whereas the 5.0 mol.% M-TiO_2 curve intensities were weakened dramatically. The decreasing tendency was observed in the following order: TiO_2 > 5.0 mol.% Fe-TiO_2 > Cu-TiO_2 > Ni-TiO_2 > Co-TiO_2, which was possibly due to the new oxygen vacancies produced by metal-doping. The photogenerated electrons in the conduction band initially reached the vacant space and then recombined with the photogenerated holes in the valance band to produce fluorescence emission. The reduced PL intensities of 5.0 mol.% M-TiO_2 might be due to defects generated by the transition metal ions inserted into the TiO_2 structures, which accelerate electron transfer and hinder electron-hole pair recombination on the 5.0 mol.% M-TiO_2 surface.

Figure 5 shows the adsorption-desorption isotherm curves of N_2 at 77 K for the as-synthesized 5.0 mol.% M (Fe-, Co-, Ni-, and Cu-) TiO_2 particles. With the exception of the 5.0 mol.% Fe-TiO_2 and Cu-TiO_2 samples, all isotherms were close to type II according to the IUPAC classification [36], indicating the lack of pores in the particles. Otherwise, the isotherms of the 5.0 mol.% Fe-TiO_2 and Cu-TiO_2 samples were attributed to type IV, indicating bulk pores by aggregation between each nanoparticle. The hysteresis slopes were observed at intermediate and relative pressures greater than $p/p_0 = 0.7$ in all samples.

Table 1 lists the specific surface areas of the 5.0 mol.% M-TiO_2 samples. The specific surface areas were located in the range 68~165 $m^2\ g^{-1}$. In particular, the surface area was the largest at 165 $m^2\ g^{-1}$ in 5.0 mol.% Fe-TiO_2. In general, the surface area increases with decreasing particle size [37]. These results showed some degree of reliability and were well matched to their calculated crystallite sizes (Figure 2). From the results of the average bulk pore diameter for the samples, it is believed that the 5.0 mol.% Fe-TiO_2 and Cu-TiO_2 may contain bulk mesopores, approximately 15~24 nm, due to aggregation between their nanoparticles. Otherwise, the pore volumes of the samples were varied from 0.17 to 0.64 $cm^3\ g^{-1}$. The atomic compositions calculated the energy-dispersive X-ray spectra that are also included in this table. The TiO_2 surface showed only two elements, Ti and O, whereas three elements were observed in the M-TiO_2 samples. In contrast to expectations, the amount of doped metals was much higher than the Ti amount in all samples, and the M : Ti ratios were approximately 1 : 10. This was calculated from EDAX analysis, and the values were different from the actual amount. The amount of metal doped in TiO_2 was reduced to the order of Fe > Co > Ni > Cu.

During the CO_2 photoreduction reaction, CO_2 is adsorbed onto the surface of the photocatalysts in the first step, and the photoreduction reaction progresses. Therefore, the photocatalytic performance depends on the adsorption capacities of CO_2. Accordingly, the CO_2 adsorption abilities of the 5.0 mol.% M (Fe-, Co-, Ni-, and Cu-) TiO_2 samples need to be determined. The CO_2 desorption profiles were obtained over the range 50~900°C, as shown in Figure 6. The curve intensity for CO_2 desorption was higher in 5.0 mol.% M-TiO_2 than in pure TiO_2, which means considerably more CO_2 molecules had been adsorbed on the surfaces of the 5.0 mol.% M-TiO_2 samples. In addition, TiO_2 generally has

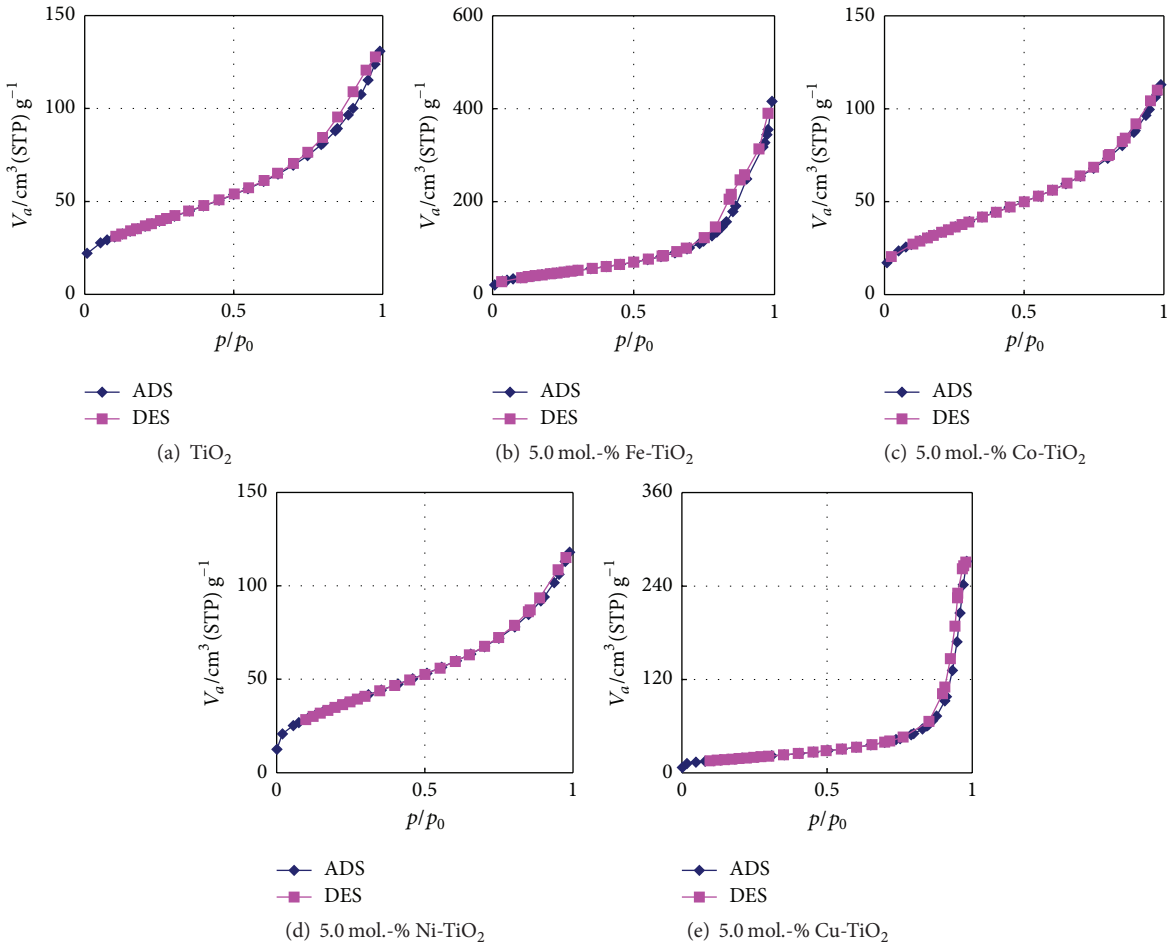

FIGURE 5: Adsorption-desorption isotherm curves of N_2 at 77 K for the as-synthesized 5.0 mol.% M-TiO_2 particles.

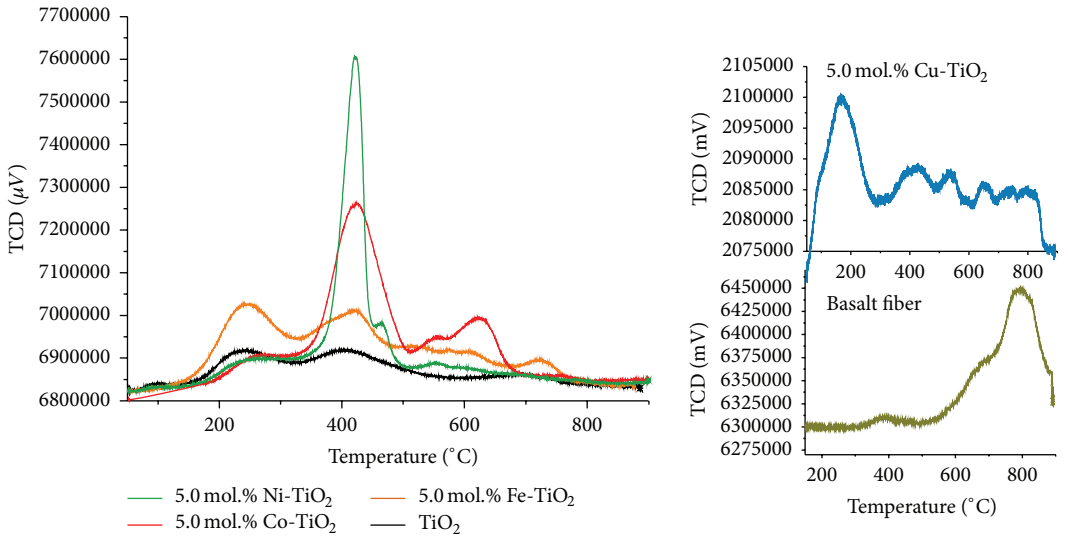

	Basalt fiber	TiO_2	5.0 mol.% Fe-TiO_2	5.0 mol.% Co-TiO_2	5.0 mol.% Ni-TiO_2	5.0 mol.% Cu-TiO_2
Area integ. (Gaussian)	27,983,665	33,278,233	66,855,506	68,781,188	60,435,286	10,310,403

FIGURE 6: CO_2 desorption profiles over the 5.0 mol.% M-TiO_2 particles in the range, 50~900°C.

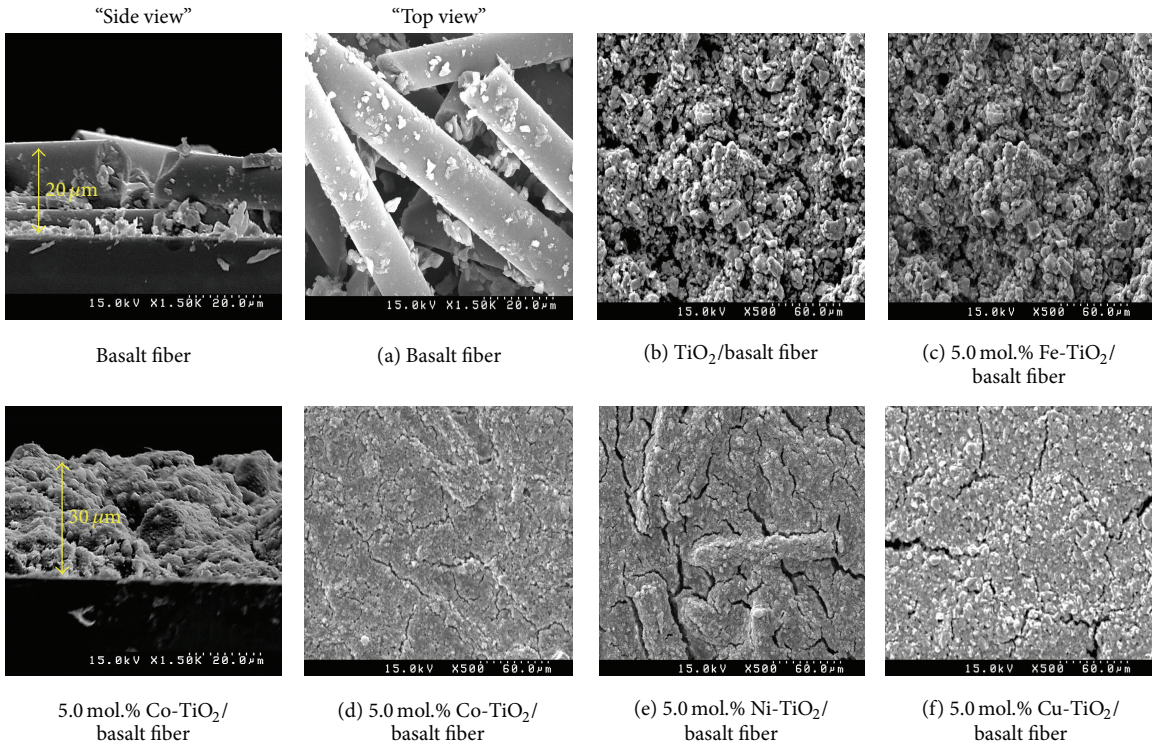

Figure 7: SEM images of the pure basalt fiber film and 5.0 mol.% M-TiO_2/basalt fiber films.

hydrophilic properties [38], which suggests that, during the CO_2 photoreduction reaction, CO_2 and H_2O will be adsorbed preferentially on the metal ions and TiO_2, respectively. The adsorption abilities were observed in the following order: 5.0 mol.% Co-TiO_2 > Ni-TiO_2 > Fe-TiO_2 > TiO_2 > Cu-TiO_2 samples. In general, a rapid catalytic reaction occurs when many reactants are well-adsorbed over the catalyst. The presence of transition metals in the 5.0 mol.% M-TiO_2 samples most likely caused the relative increase in the number of CO_2 and H_2O molecules adsorbed compared to pure TiO_2. This synergy contributed significantly to improving the catalytic performance of the 5.0 mol.% M-TiO_2 samples.

3.2. Characteristics and CO_2 Photoreduction over the 5.0 mol.% M (Fe-, Co-, Ni-, and Cu-) TiO_2/Basalt Fiber Films. Figure 7 presents SEM images (top and side views) of the six samples of pure basalt fiber and TiO_2 films and 5.0 mol.% M (Fe-, Co-, Ni-, and Cu-) TiO_2/basalt fiber films. The basalt fiber in the films was approximately 15 μm in diameter with different lengths and the surfaces were smooth. The 5.0 mol.% M-TiO_2 materials were mixed with basalt fibers and were fabricated as thick films by coating on a Pyrex plate. The regular array of composites could be observed clearly through both the side and top directions. The TiO_2/basalt fiber and 5.0 mol.% Fe-TiO_2/basalt fiber composites did not cover the Pyrex plate surface completely, and bulk pores were observed. On the other hand, the coating parts were quite uniform and fine particles were well-dispersed. In contrast, the surfaces of the films fabricated from 5.0 mol.% Co-TiO_2/basalt fiber, 5.0 mol.% Ni-TiO_2/basalt fiber, and 5.0 mol.% Cu-TiO_2/basalt fiber composites were quite dense, despite containing some cracks. In particular, the surface was the most compact over the 5.0 mol.% Co-TiO_2/basalt fiber film. The thickness of the films in all samples was approximately 30~35 μm with the exception of the pure basalt fiber film (20 μm).

Energy-dispersive X-ray spectroscopy (EDAX) confirmed the presence of metals on the surfaces of the basalt fiber and 5.0 mol.% M (Fe-, Co-, Ni-, and Cu-) TiO_2/basalt fiber films, as shown in Figure 8, and the table below lists the atomic compositions determined by EDAX. For the basalt fiber, various metal oxides were observed, such as Na, K, Ca, Mg, Al, Si, Fe, and Ti. Pure basalt fiber exhibited a composition of 19.28 wt.% Si, 3.14 wt.% total alkali metals, 1.66 wt.% Ti, 11.77 wt.% Fe, and 5.61 wt.% Al. As a CO_2 adsorbent, the Ca and Mg contents were 5.31 and 2.09 wt.%, respectively. Ti contained on the 5.0 mol.% M (Fe-, Co-, Ni-, and Cu-) TiO_2/basalt fiber films decreased in the following order: 5.0 mol.% Ni-TiO_2 (47.74 wt.%) > Co-TiO_2 (42.68 wt.%) > TiO_2 (40.94 wt.%) > Fe-TiO_2 (33.44 wt.%). The amounts of transition metal species were in the range 2.69 to 3.02 wt.%, with the exception of copper (0.98 wt.%). These values did not appear to be perfectly quantitative: EDAX is a very good surface analytical method but it is prone to error because the composition can vary according to the location. In particular, the variation is large when the sample is nonuniform [39].

The efficiencies of the photogenerated electron-hole production in the basalt fiber and 5.0 mol.% M (Fe-, Co-, Ni-,

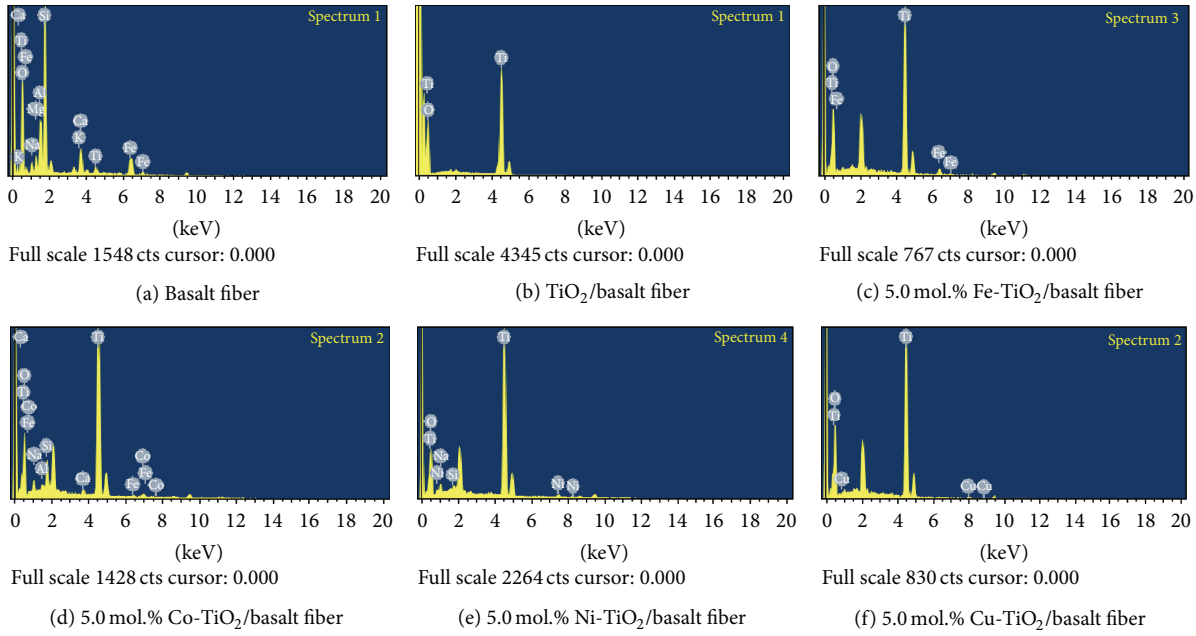

Materials/element	Atomic compositions (wt.-%)											
	O	Na	Mg	Al	Si	K	Ca	Ti	Fe	Co	Ni	Cu
(a)	51.14	2.04	2.09	5.61	19.28	1.10	5.31	1.66	11.77	—	—	—
(b)	59.06	—	—	—	—	—	—	40.94	—	—	—	—
(c)	41.22	—	—	—	—	—	—	33.44	2.86	—	—	—
(d)	48.03	1.92	—	0.59	2.28	—	0.66	42.68	1.14	2.69	—	—
(e)	47.32	1.60	—	—	0.32	—	—	47.74	—	—	3.02	—
(f)	45.43							36.15				0.98

FIGURE 8: Energy-dispersive X-ray spectra of the surfaces of the pure basalt fiber and 5.0 mol.% M-TiO_2/basalt fiber films and the atomic compositions.

and Cu-) TiO_2/basalt fiber films were measured from the photocurrent response under solar light irradiation at an applied potential of 0.7 V versus SCE. Figure 9 shows the typical real time photocurrent response of the films when the light source is switched on and off, exhibiting a rapid photocurrent rise and decay. In semiconductor systems, when irradiation provides an energy higher than the band-gap of a semiconductor, the energy excites an electron from the valence band to the conduction band, leaving a hole in the valence band. The electron-hole pair is responsible for the photocurrent. When the light was turned on, a rapid increase in the photoreduction current was observed, and the photocurrent then turned to a steady state after a few seconds. When the light was turned off, the photocurrent decreased instantaneously to almost zero [40]. When the light was turned on, the maximum photocurrents obtained for the 5.0 mol.% Co-TiO_2/and Ni-TiO_2/basalt fiber films were 310.49 and 300.75 mA cm^{-2}, respectively, which were more than four times higher than that achieved on pure basalt fiber (71.23 mA cm^{-2}) and TiO_2/basalt fiber films (74.01 mA cm^{-2}). The maximum photocurrent of the 5.0 mol.% Cu-TiO_2/basalt fiber film was too small due to trapping of excited electrons by copper with strong oxidation agency. In addition, the TiO_2/basalt fiber, 5.0 mol.% Cu-TiO_2/basalt fiber, and 5.0 mol.% Ni-TiO_2/basalt fiber films showed no current transients in both the light-on and the light-off regions in the samples falling off with time in 50 s to a steady state, which indicates that few surface recombination processes had occurred. Clearly, some electron-hole recombination was observed in the 5.0 mol.% Fe-TiO_2/basalt fiber and Co-TiO_2/basalt fiber films, but it was negligible compared to the total current value. Therefore, the 3d-transition metal ingredients have a beneficial effect on the photocurrent; it plays a role as an intermediate for the efficient separation of photogenerated hole-electron pairs.

Figure 10 presents the photoreduction abilities of CO_2 with H_2O vapor to CH_4 over the pure basalt fiber film and 5.0 mol.% M (Fe-, Co-, Ni-, and Cu-) TiO_2/basalt fiber films

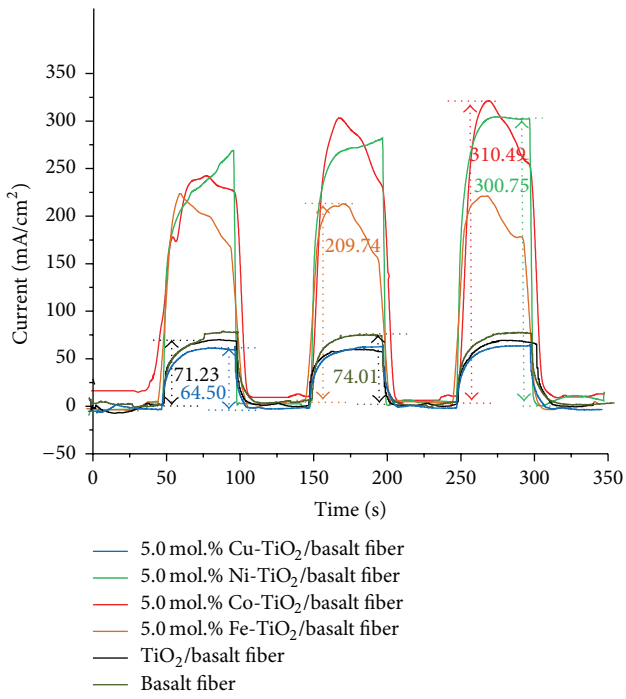

FIGURE 9: Photocurrent responses of the pure basalt fiber and 5.0 mol.% M-TiO_2/basalt fiber films when the light source was switched on and off.

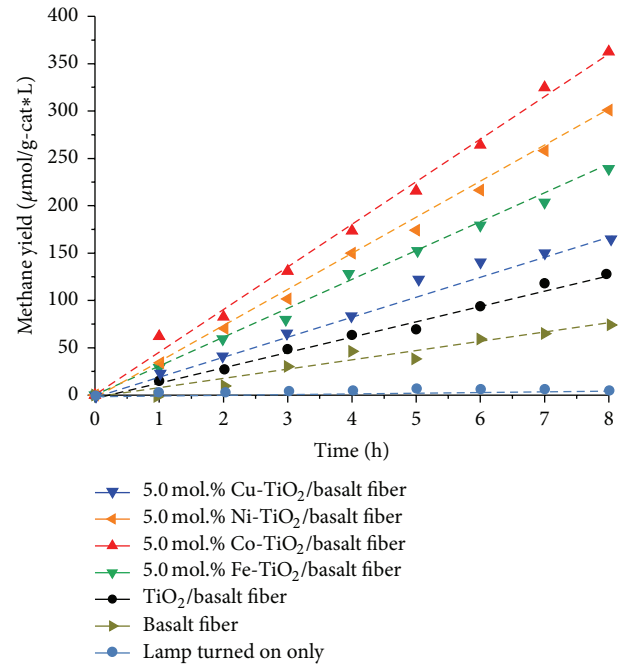

FIGURE 10: Photoreduction abilities of CO_2 with H_2O vapor to CH_4 over the pure basalt fiber film and 5.0 mol.% M-TiO_2/basalt fiber films after 8 h.

after 8 h. Generally, CH_4 production from CO_2 reduction with H_2O can be divided into the following three subprocesses [41]: proton production from H_2O photodecomposition, CO radical production from CO_2 photo cleavage, and methane production from photosynthesis between the CO radical and proton. The photogenerated electrons on the photocatalysts by UV-radiation induce CO_2 reduction to produce CO_2 radicals, whereas the holes react with the adsorbed H_2O molecules to perform oxidation. The intermediate photogenerated species undergo different reactions to produce CO, CH_3OH, and CH_4. The production of CH_4 from methyl radicals ($^{\bullet}CH_3$) was confirmed, which are dependent directly on the formation of the intermediate product, CO [42]. As shown in this figure, almost no methane was observed when only the lamp was turned on. On the other hand, the amounts of CO and O_2 generation increased, and a small amount of hydrogen was observed. This means that the light does not induce photoreduction processes alone. On the other hand, there are different product distributions according to the loaded metal species: excessive methane is generated over the catalysts loaded with Ni and Co, and the quantities of CO and CH_3OH gases are increased over the catalysts loaded with Cu and Fe. The M-TiO_2/basalt fiber films showed higher CH_4 production from CO_2 photoreduction than the pure basalt fiber and TiO_2/basalt fiber films. 70.0 μmol g_{cat}^{-1} L^{-1} CH_4 was emitted over the pure basalt fiber film, suggesting that it contains a small amount of TiO_2. On the other hand, CH_4 production was 112.1 μmol g_{cat}^{-1} L^{-1} over the TiO_2/basalt fiber film. In contrast, the maximum CH_4 yields over the 5.0 mol.% Co-TiO_2/basalt fiber and Ni-TiO_2/basalt fiber films were 360.5 and 307.3 μmol g_{cat}^{-1} L^{-1}, respectively. The differences in yields were attributed to their band-gaps, electron-hole recombination tendencies, and the gas adsorption abilities of the 5.0 mol.% M-TiO_2/basalt fiber films. In particular, this study confirmed that the 5.0 mol.% Co-TiO_2 particles show synergistic performance when the basalt fiber is mixed.

The reduction of CO_2 requires a multiple electron transfer and leads to production of a variety of products, depending on the number of transferred electrons, which determine the final oxidation state of the carbon atom. The standard redox potentials of the CO_2 reduction half-reactions vary from CO_2/HCOOH [43] to CO_2/CH_4 [44]: CO_2 adsorbed on a photocatalyst surface can be reduced to $^{\bullet}CO_2^-$ anion radical, which can react with H^+ and e^- for forming HCOOH or $HCOO^-$ or which can go to the postulated disproportionation reaction of two $^{\bullet}CO_2^-$ anion radicals into CO (after all to be C radical) and CO_3^{2-} to react with H radical. This study seems to follow the latter. Scheme 1 presents a model for CO_2 photoreduction over the M-TiO_2/basalt fiber films based on the relationships between the optical properties of the photocatalysts and the catalytic activities. Photon excitation in M-TiO_2 over the M-TiO_2/basalt fiber films will begin rapidly because M-TiO_2 has a shorter band-gap than pure TiO_2, and the excited electrons can be transferred efficiently to CO_2 molecules. In addition, CO_2 molecules are adsorbed preferentially and easily on the basalt fiber surface. The positive holes on the valance band of M-TiO_2 can be trapped by H_2O species and transferred to OH radicals and protons. The protons obtained are transformed to H

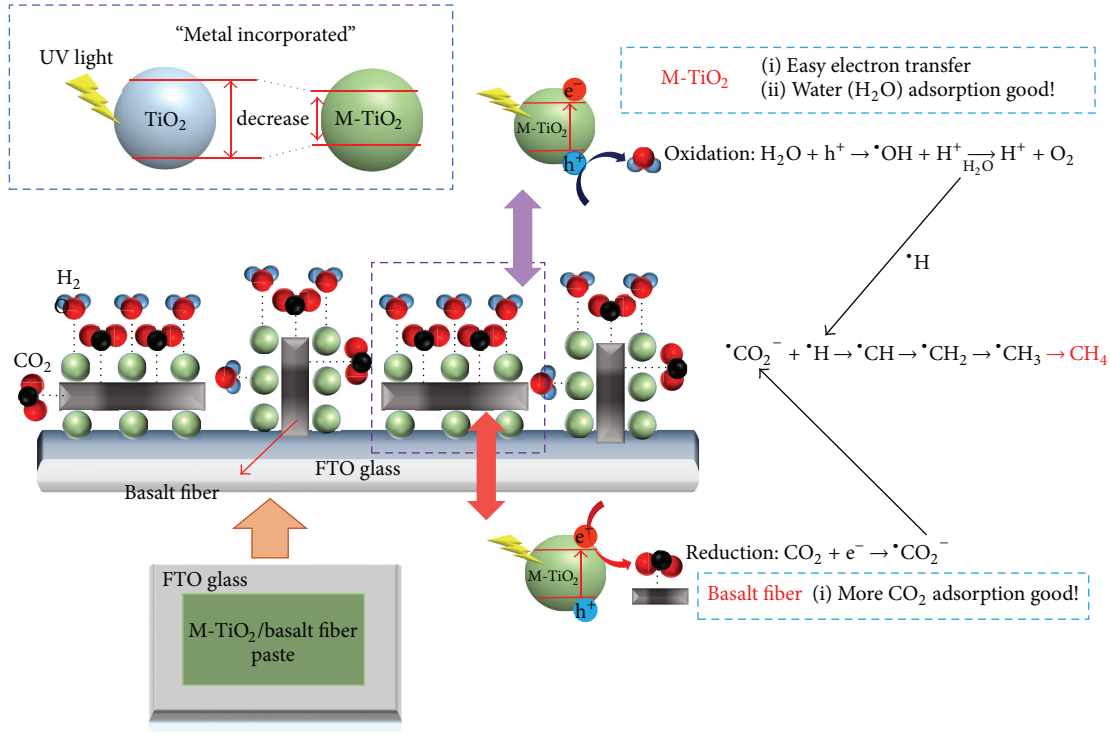

Scheme 1: Model for CH_4 production from the photoreduction of CO_2 with H_2O vapor over the M-TiO_2/basalt fiber films.

radicals by electrons, and the H radicals then react with C and CO radicals formed from the reduction of CO_2^- over M-TiO_2, particularly over Co- or Ni-TiO_2 semiconductors, resulting methane production [45]. The mixed films of basalt fibers and M-TiO_2 can also promote the separation of photogenerated electron-hole pairs (e^-/h^+) on M-TiO_2. Therefore, the synergetic effects of the basalt fibers and M-TiO_2 in the M-TiO_2/basalt fiber films achieved higher CO_2 reduction efficiency.

4. Conclusions

The 5.0 mol.% M (Fe-, Co-, Ni-, and Cu-) incorporated TiO_2 photocatalysts obtained by the solvothermal method were coated densely with basalt fibers on a Pyrex plate using a squeeze technique and applied to the photoreduction of CO_2 to CH_4. The CO_2 adsorption abilities were improved over the basalt fiber, and CH_4 generation was enhanced dramatically over 5.0 mol.% M-TiO_2/basalt fiber films with a threefold higher yield compared to the pure basalt fiber and TiO_2/basalt fiber films. In particular, the photoreduction of CO_2 with H_2O revealed a remarkable increase in CH_4 generation over the 5.0 mol.% Co-TiO_2/basalt fiber film to 360.5 μmol $g_{cat}^{-1} \cdot L^{-1}$ after an 8 h reaction.

Competing Interests

The authors declare that they have no competing interests.

Acknowledgments

This research was supported by ceramic fiber commercial center project of Korea Institute of Ceramic Engineering & Technology (KICET) funded by the Ministry of Trade, Industry & Energy (MOTIE).

References

[1] M. Tahir and N. S. Amin, "Indium-doped TiO_2 nanoparticles for photocatalytic CO_2 reduction with H_2O vapors to CH_4," *Applied Catalysis B: Environmental*, vol. 162, pp. 98–109, 2015.

[2] B. S. Kwak and M. Kang, "Photocatalytic reduction of CO_2 with H_2O using perovskite $Ca_xTi_yO_3$," *Applied Surface Science*, vol. 337, pp. 138–144, 2015.

[3] C. Fletcher, Y. Jiang, and R. Amal, "Production of formic acid from CO_2 reduction by means of potassium borohydride at ambient conditions," *Chemical Engineering Science*, vol. 137, pp. 301–307, 2015.

[4] G. Mahmodi, S. Sharifnia, M. Madani, and V. Vatanpour, "Photoreduction of carbon dioxide in the presence of H_2, H_2O and CH_4 over TiO_2 and ZnO photocatalysts," *Solar Energy*, vol. 97, pp. 186–194, 2013.

[5] J. Albo, A. Sáez, J. Solla-Gullón, V. Montiel, and A. Irabien, "Production of methanol from CO_2 electroreduction at Cu_2O and Cu_2O/ZnO-based electrodes in aqueous solution," *Applied Catalysis B: Environmental*, vol. 176-177, pp. 709–717, 2015.

[6] P. Akhter, M. Hussain, G. Saracco, and N. Russo, "New nanostructured silica incorporated with isolated Ti material for the

photocatalytic conversion of CO_2 to fuels," *Nanoscale Research Letters*, vol. 9, article 158, 2014.

[7] M. Anpo, "Photocatalytic reduction of CO_2 with H_2O on highly dispersed Ti-oxide catalysts as a model of artificial photosynthesis," *Journal of CO_2 Utilization*, vol. 1, pp. 8–17, 2013.

[8] H. Abdullah, M. R. Khan, M. Pudukudy, Z. Yaakob, and N. A. Ismail, "CeO_2-TiO_2 as a visible light active catalyst for the photoreduction of CO_2 to methanol," *Journal of Rare Earths*, vol. 33, no. 11, pp. 1155–1161, 2015.

[9] O. Ola and M. Mercedes Maroto-Valer, "Review of material design and reactor engineering on TiO_2 photocatalysis for CO_2 reduction," *Journal of Photochemistry and Photobiology C: Photochemistry Reviews*, vol. 24, pp. 16–42, 2015.

[10] X. Zhang, L. Wang, Q. Du, Z. Wang, S. Ma, and M. Yu, "Photocatalytic CO_2 reduction over B_4C/C_3N_4 with internal electric field under visible light irradiation," *Journal of Colloid and Interface Science*, vol. 464, pp. 89–95, 2016.

[11] R. Gusain, P. Kumar, O. P. Sharma, S. L. Jain, and O. P. Khatri, "Reduced graphene oxide-CuO nanocomposites for photocatalytic conversion of CO_2 into methanol under visible light irradiation," *Applied Catalysis B: Environmental*, vol. 181, pp. 352–362, 2016.

[12] N. M. Nursam, X. Wang, and R. A. Caruso, "High-throughput synthesis and screening of titania-based photocatalysts," *ACS Combinatorial Science*, vol. 17, no. 10, pp. 548–569, 2015.

[13] M. V. Dozzi, S. Marzorati, M. Longhi, M. Coduri, L. Artiglia, and E. Selli, "Photocatalytic activity of TiO_2-WO_3 mixed oxides in relation to electron transfer efficiency," *Applied Catalysis B: Environmental*, vol. 186, pp. 157–165, 2016.

[14] Y. Qu and X. Duan, "Progress, challenge and perspective of heterogeneous photocatalysts," *Chemical Society Reviews*, vol. 42, no. 7, pp. 2568–2580, 2013.

[15] J. C. Colmenares, R. Luque, J. M. Campelo, F. Colmenares, Z. Karpiński, and A. A. Romero, "Nanostructured photocatalysts and their applications in the photocatalytic transformation of lignocellulosic biomass: an overview," *Materials*, vol. 2, no. 4, pp. 2228–2258, 2009.

[16] M. Kitano, M. Matsuoka, M. Ueshima, and M. Anpo, "Recent developments in titanium oxide-based photocatalysts," *Applied Catalysis A: General*, vol. 325, no. 1, pp. 1–14, 2007.

[17] P. Silija, Z. Yaakob, V. Suraja, N. N. Binitha, and Z. S. Akmal, "An enthusiastic glance in to the visible responsive photocatalysts for energy production and pollutant removal, with special emphasis on titania," *International Journal of Photoenergy*, vol. 2012, Article ID 503839, 19 pages, 2012.

[18] H. Xu, S. Ouyang, L. Liu, P. Reunchan, N. Umezawa, and J. Ye, "Recent advances in TiO_2-based photocatalysis," *Journal of Materials Chemistry A*, vol. 2, no. 32, pp. 12642–12661, 2014.

[19] Z. He, J. Tang, J. Shen, J. Chen, and S. Song, "Enhancement of photocatalytic reduction of CO_2 to CH_4 over TiO_2 nanosheets by modifying with sulfuric acid," *Applied Surface Science*, vol. 364, pp. 416–427, 2016.

[20] O. Ola and M. M. Maroto-Valer, "Transition metal oxide based TiO_2 nanoparticles for visible light induced CO_2 photoreduction," *Applied Catalysis A: General*, vol. 502, pp. 114–121, 2015.

[21] D. Eder, "Carbon nanotube-inorganic hybrids," *Chemical Reviews*, vol. 110, no. 3, pp. 1348–1385, 2010.

[22] L. Zhang, R. Jamal, Q. Zhao, M. Wang, and T. Abdiryim, "Preparation of PEDOT/GO, PEDOT/MnO_2, and PEDOT/GO/MnO_2 nanocomposites and their application in catalytic degradation of methylene blue," *Nanoscale Research Letters*, vol. 10, p. 148, 2015.

[23] M. Urbanski, A. Lapko, and A. Garbacz, "Investigation on concrete beams reinforced with basalt rebars as an effective alternative of conventional R/C structures," *Procedia Engineering*, vol. 57, pp. 1183–1191, 2013.

[24] S. A. Chernyak, E. V. Suslova, A. V. Egorov, L. Lu, S. V. Savilov, and V. V. Lunin, "New hybrid CNT-alumina supports for Co-based Fischer-Tropsch catalysts," *Fuel Processing Technology*, vol. 140, pp. 267–275, 2015.

[25] K. Shimura, T. Miyazawa, T. Hanaoka, and S. Hirata, "Fischer–Tropsch synthesis over alumina supported bimetallic Co–Ni catalyst: effect of impregnation sequence and solution," *Journal of Molecular Catalysis A: Chemical*, vol. 407, pp. 15–24, 2015.

[26] F. Fazlollahi, M. Sarkari, A. Zare, A. A. Mirzaei, and H. Atashi, "Development of a kinetic model for Fischer-Tropsch synthesis over Co/Ni/Al_2O_3 catalyst," *Journal of Industrial and Engineering Chemistry*, vol. 18, no. 4, pp. 1223–1232, 2012.

[27] J. Zhao, W. Xing, Y. Li, and K. Lu, "Solvothermal synthesis and visible light absorption of anatase TiO_2," *Materials Letters*, vol. 145, pp. 332–335, 2015.

[28] S. Liu, J. Yu, and M. Jaroniec, "Anatase TiO_2 with dominant high-energy 001 facets: Synthesis, properties, and applications," *Chemistry of Materials*, vol. 23, no. 18, pp. 4085–4093, 2011.

[29] T. Ungár, "Microstructural parameters from X-ray diffraction peak broadening," *Scripta Materialia*, vol. 51, no. 8, pp. 777–781, 2004.

[30] A. W. Burton, K. Ong, T. Rea, and I. Y. Chan, "On the estimation of average crystallite size of zeolites from the Scherrer equation: a critical evaluation of its application to zeolites with one-dimensional pore systems," *Microporous and Mesoporous Materials*, vol. 117, no. 1-2, pp. 75–90, 2009.

[31] A. Jaroenworaluck, N. Pijarn, N. Kosachan, and R. Stevens, "Nanocomposite TiO_2–SiO_2 gel for UV absorption," *Chemical Engineering Journal*, vol. 181-182, pp. 45–55, 2012.

[32] J. I. Peña-Flores, A. F. Palomec-Garfias, C. Márquez-Beltrán, E. Sánchez-Mora, E. Gómez-Barojas, and F. Pérez-Rodríguez, "Fe effect on the optical properties of TiO_2:Fe_2O_3 nanostructured composites supported on SiO_2 microsphere assemblies," *Nanoscale Research Letters*, vol. 9, article 499, 2014.

[33] D. Kim, Y. Im, K. M. Jeong, S.-M. Park, M.-H. Um, and M. Kang, "Enhanced 2-chorophenol photodecomposition using nano-sized Mn-incorporated TiO_2 powders prepared by a solvothermal method," *Bulletin of the Korean Chemical Society*, vol. 35, no. 8, pp. 2295–2298, 2014.

[34] C. C. Huang, C. C. Wu, K. Knight, and D. W. Hewak, "Optical properties of CVD grown amorphous Ge-Sb-S thin films," *Journal of Non-Crystalline Solids*, vol. 356, no. 4-5, pp. 281–285, 2010.

[35] J. Kim, J. S. Lee, and M. Kang, "Synthesis of nanoporous structured SnO_2 and its photocatalytic ability for bisphenol a destruction," *Bulletin of the Korean Chemical Society*, vol. 32, no. 5, pp. 1715–1720, 2011.

[36] M. Thommes, "Physical adsorption characterization of nanoporous materials," *Chemie Ingenieur Technik*, vol. 82, no. 7, pp. 1059–1073, 2010.

[37] A. A. Gribb and J. F. Banfield, "Particle size effects on transformation kinetics and phase stability in nanocrystalline TiO_2," *American Mineralogist*, vol. 82, no. 7-8, pp. 717–728, 1997.

[38] S.-H. Nam, S.-J. Cho, C.-K. Jung et al., "Comparison of hydrophilic properties of TiO_2 thin films prepared by sol–gel method and reactive magnetron sputtering system," *Thin Solid Films*, vol. 519, no. 20, pp. 6944–6950, 2011.

[39] H. G. Feichtinger, K. Gröchenig, and T. Strohmer, "Efficient numerical methods in non-uniform sampling theory," *Numerische Mathematik*, vol. 69, no. 4, pp. 423–440, 1995.

[40] S. W. Jo, B. S. Kwak, K. M. Kim et al., "Effectively CO_2 photoreduction to CH_4 by the synergistic effects of Ca and Ti on Ca-loaded TiSiMCM-41 mesoporous photocatalytic systems," *Applied Surface Science*, vol. 355, pp. 891–901, 2015.

[41] J. Y. Do, Y. Im, B. S. Kwak, J.-Y. Kim, and M. Kang, "Dramatic CO_2 photoreduction with H_2O vapors for CH_4 production using the TiO_2 (bottom)/Fe–TiO_2 (top) double-layered films," *Chemical Engineering Journal*, vol. 275, pp. 288–297, 2015.

[42] M. Tahir and N. Saidina Amin, "Photocatalytic reduction of carbon dioxide with water vapors over montmorillonite modified TiO_2 nanocomposites," *Applied Catalysis B: Environmental*, vol. 142-143, pp. 512–522, 2013.

[43] Y. Kohno, H. Hayashi, S. Takenaka, T. Tanaka, T. Funabiki, and S. Yoshida, "Photo-enhanced reduction of carbon dioxide with hydrogen over Rh/TiO_2," *Journal of Photochemistry and Photobiology A: Chemistry*, vol. 126, no. 1–3, pp. 117–123, 1999.

[44] M. Subrahmanyam, S. Kaneco, and N. Alonso-Vante, "A screening for the photo reduction of carbon dioxide supported on metal oxide catalysts for C_1-C_3 selectivity," *Applied Catalysis B: Environmental*, vol. 23, no. 2-3, pp. 169–174, 1999.

[45] S. S. Tan, L. Zou, and E. Hu, "Kinetic modelling for photosynthesis of hydrogen and methane through catalytic reduction of carbon dioxide with water vapour," *Catalysis Today*, vol. 131, no. 1–4, pp. 125–129, 2008.